



# Syn- and post-eruptive gully formation near the Laacher See volcano

Max Engel<sup>1</sup>  | Markus Dotterweich<sup>2</sup> | Alexander Fülling<sup>3</sup> | Dominik Brill<sup>4</sup>  |  
Manuela Broisch-Höhner<sup>5</sup> | Ralf Totschnig<sup>6</sup> | Sirri Seren<sup>6</sup> | Martin Kehl<sup>4</sup> 

<sup>1</sup>Institute of Geography, Heidelberg University, Heidelberg, Germany

<sup>2</sup>UDATA GmbH, Neustadt an der Weinstraße, Germany

<sup>3</sup>Institute of Earth and Environmental Sciences, University of Freiburg, Freiburg, Germany

<sup>4</sup>Institute of Geography, University of Cologne, Cologne, Germany

<sup>5</sup>ArchaeoGeophysics, Institute of Archaeology, University of Cologne, Cologne, Germany

<sup>6</sup>Department of Geophysics, Zentralanstalt für Meteorologie und Geodynamik (ZAMG), Vienna, Austria

## Correspondence

Max Engel, Institute of Geography, Heidelberg University, Im Neuenheimer Feld 348, 69120 Heidelberg, Germany.  
Email: max.engel@uni-heidelberg.de

## Funding information

University of Cologne; Deutsche Forschungsgemeinschaft

## Abstract

The Laacher See volcano (LSV) is located at the western margin of the Neuwied Basin, the central part of the Middle Rhine Basin of Germany. Its paroxysmal Plinian eruption c. 13 ka ago (Laacher See event; LSE) deposited a complex tephra sequence in the Neuwied Basin, whilst the distal ashes became one of the most important chronostratigraphic markers in Central Europe. However, some other impacts on landscape formation have thus far been largely neglected, such as buried gully structures in the proximity of the LSV. In this contribution, we map and discuss the spatial extent of these landforms at the site Lungenkärchen c. 4 km south of the LSV based on geophysical prospection as well as contrasting pedo-sedimentary characteristics of the gully infill (particle-size distribution, bulk-sediment density, thin-section analysis, saturated hydraulic conductivity) and the surrounding soils and tephra layers. These data are combined with a luminescence- and carbon-14 (<sup>14</sup>C)-based age model that relates them to the LSE. It is demonstrated how these gullies seem to have been formed and rapidly infilled by rainfall and surface discharge both during and subsequent to the eruptive phase, with modern analog processes documented for the 1980 Mount St Helens eruption (Washington State, USA). Given the density of the gullies at the site and their deviating pedo-sedimentary properties compared to the surrounding soils, we propose a significant influence on agricultural production in the proximity of the LSV, which remains to be tested in future studies. Finally, in contrast, gullies of similar lateral and vertical dimensions identified in post-LSE reworked loess and tephra deposits of the Wingertsbergwand (close to the main study site and proximal to the LSV) have shown to be unrelated to the LSE and can either be attributed to periglacial processes at the Younger Dryas-Preboreal transition or to linear incision during the early Holocene.

## KEYWORDS

Eifel, ground-penetrating radar (GPR), gully erosion, Laacher See event (LSE), luminescence dating, magnetometer prospection, micromorphology, tephra, Wingertsbergwand

## 1 | INTRODUCTION

The Laacher See volcano (LSV) at the western margin of the Neuwied Basin is part of the Volcanic Eifel (Rhineland-Palatinate, Germany) (Figure 1). Its paroxysmal Plinian eruption c. 13 ka ago

(Reinig et al., 2020) was nourished by a highly stratified magma chamber and controlled by a variety of volcanic and other environmental factors. These include the aquifer level, crustal lithology, the volcano-tectonic alignment, as well as vent widening, collapse, downward erosion, and migration (Schmincke et al., 1999).

This is an open access article under the terms of the Creative Commons Attribution License, which permits use, distribution and reproduction in any medium, provided the original work is properly cited.

© 2021 The Authors. *Earth Surface Processes and Landforms* published by John Wiley & Sons Ltd.

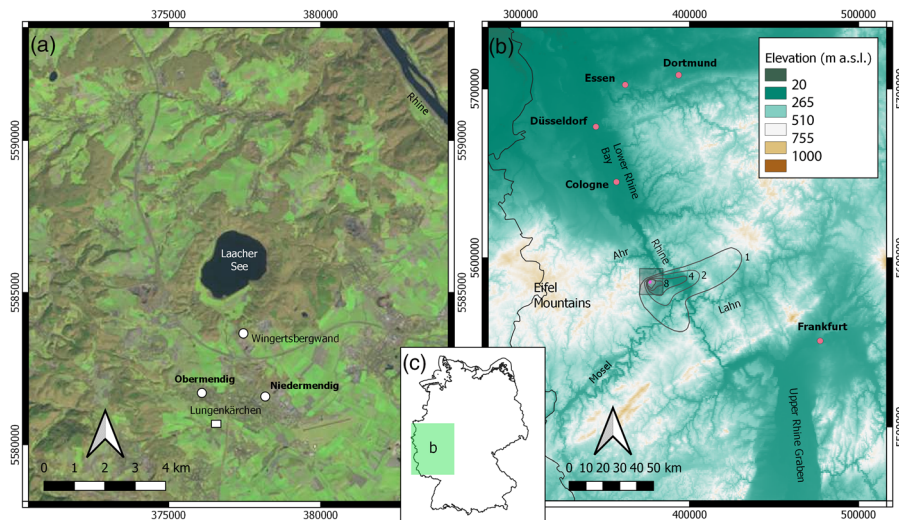


**FIGURE 1** (a) Spatial context of the core study site “Lungenkärchen” (white rectangle indicates location of the maps in Figure 2), the Wingertsbergwand and the Laacher See (based on Landsat 8 data, courtesy of US Geological Survey [USGS], 2013). (b) Wider regional context of the study area (dark grey, semi-transparent rectangle represents the map in (a)), including the location of the Laacher See (magenta) and isopachs of depositional thickness of Laacher See tephra in meters after Schmincke *et al.* (1999) (based on GTOPO30 dataset, courtesy of USGS, 1996). For both maps (a) and (b), the transverse Mercator projection is applied; coordinates represent UTM zone 32N. (c) Location of map (b)

Two thirds of the compositionally zoned phonolitic magma volume of c.  $6.3 \text{ km}^3$  were erupted within a period of 10 h (Litt *et al.*, 2003). The ejecta comprised mainly lapilli tephra, but also tremendous amounts of ashes were distributed in three primary directions of propagation across Central Europe (Figure 1b). The Laacher See event (LSE) had a significant impact on topography and regional soils (Schmincke *et al.*, 1999; Nowell *et al.*, 2006; Hahn & Opp, 2011; Schmincke, 2014; Viereck, 2019), and triggered temporary lake reservoir formation in the Neuwied Basin with catastrophic dam outburst towards the end of the event (e.g., Schmincke *et al.*, 1999; Litt *et al.*, 2003).

One peculiar geomorphic feature associated with tephra deposits of the LSE has remained unstudied so far, that is gullies, which are up to a few meters wide and up to c. 2 m deep. Gully formation in central-western Europe has been usually associated with combined anthropogenic land degradation and intense rainfalls over timescales of decades up to centuries, in particular during the 14th and 18th centuries (e.g., Vanwallegghem *et al.*, 2005; Lang & Mauz, 2006; Stolz & Grunert, 2006; Dotterweich, 2008, 2013). In some very specific cases, large gullies have been associated with single paroxysmal rainfall events, such as the one of 1342 (Bork *et al.*, 2006a; Dotterweich, 2008). The gullies incised into the tephra of the LSE seem to have also formed very rapidly. They occur at prominent proximal tephra sequences, such as the Wingertsbergwand (WBW) immediately south of the LSV (Schmincke, 2014). Yet, very few data are available about their spatial extent, density and occurrence pattern in the wider area of the LSV. The present contribution addresses this knowledge gap and, for the very first time, documents the lateral distribution and stratigraphical context of gullies adjacent to the LSV. Based on a new geophysical, sedimentological and geochronological dataset, we test their genetical relation to the LSE and discuss further implications of eruption-related gully incision and infill for agricultural land use.

## 2 | STUDY AREA

The study area in the East Eifel region is part of the Hercynian Rhenish Massif, characterized by folded Lower Devonian schists and sandstones (Siegenium). It extends into the tectonic, intramontane Neuwied Basin, where the Palaeozoic is overlain by a sequence of Tertiary to Quaternary fluvio-lacustrine sediments (Rath, 2003; Schmincke, 2014). The Rhenish Massif was subjected to tectonic uplift, lithospheric thinning, and peneplanation since the early Palaeogene (Ilies *et al.*, 1979; Semmel, 1996; Nowell *et al.*, 2006), associated with an earlier, Eocene phase of volcanism (Nowell *et al.*, 2006). Maximum rates of uplift were reached during the Pleistocene with up to 140 m since the formation of the Main Terrace of the Middle Rhine Valley system c. 730 ka ago (Demoulin & Hallot, 2009). This gave rise to lithospheric thinning and the Pleistocene formation of the Laacher See volcanic field with c. 70 vents distributed over an area of  $400 \text{ km}^2$ . Around 700–370 ka ago, it erupted phonolitic tuffs and lavas, followed by the formation of cinder cones, basaltic volcanoes and lava flows (c. 200–100 ka ago) (Ilies *et al.*, 1979; Nowell *et al.*, 2006). The short, terminal period was characterized by phonolitic and trachytic lapilli tuffs and ashes, which were distributed over large areas (Schmincke *et al.*, 1999). The last major eruption, the LSE, is dated to around 13 ka ago (Reinig *et al.*, 2020). Massive loads of pumice tuff were emitted during this explosive event and the Laacher See caldera with a diameter of 3 km was created. Its pumice lapilli and ashes were transported over large parts of Central Europe forming a major stratigraphic marker horizon for the terminal Pleistocene (Schmincke *et al.*, 1999; Litt *et al.*, 2003; Nowell *et al.*, 2006; Schmincke, 2014). Recent gas exhalations and deep low-frequency earthquake activity beneath the Laacher See caldera may indicate active magma recharge (Hensch *et al.*, 2019).

The WBW site (Wingertsbergwand), located less than 1.5 km south of the caldera (Figure 1a; Supporting Information Figure S1),

exposes more than 30 m of highly stratified LSE deposits, which reflect various stages of the eruption. The LSE deposits are subdivided into the Lower Laacher See tephra (LLST), Middle Laacher See tephra (MLST) and Upper Laacher See tephra (ULST), representing the three main stages of the eruption, which lasted a total of a few months only. The LLST comprises a poorly sorted ash bed with plant remains and accretionary lapilli resulting from the initial phreatomagmatic explosion. This ash bed is overlain by whitish inflated pumice from the Plinian eruption. The MLST comprises a phreatomagmatic surge deposit combined with small-scale Plinian fallout units (MLST-A), loose ash-flow deposits topped by pumice lapilli (MLST-B), and dense, greyish pumice fallout layers interbedded with minor ash flows (MLST-C). The ULST consists of moderately sorted breccias with crystal-rich lapilli and dark phonolithic clasts, as well as massive ash-flow deposits (van den Boogard & Schmincke, 1985; Schmincke et al., 1999; Viereck, 2019). Cross-bedding structures within the proximal ash-flow deposit represent a radially disposed upcurrent migration of antidunes, which reflects high-velocity, cohesive phreatomagmatic flows in the range of > 100 km/h (Schmincke et al., 1973).

The main study site of Lungenkärchen in the eastern part of the Segbach Valley, immediately south of the town of Obermendig and c. 4 km south of the Laacher See, is dominated by trachytic tuff deposits. The flanks of the valley are covered by late Pleistocene slope debris and isolated volcanic ejecta (Schmincke & van den Boogard, 1990; Mangartz, 1993). A range of different soil types have formed on top of the volcanogenic loamy to sandy substrates of the Segbach Valley, dominated by brown earths and, where coarser ashes and fine lapilli dominate, regosols (*sensu* Food and Agriculture Organization of the United Nations [FAO] and German soil systematics). The narrow floodplain is characterized by gleysols and vegas (Beck, 2003). The main study site covers an area of c. 7 ha at the archaeological site of Lungenkärchen in the eastern Segbach Valley (Figure 1a). At this site, a Roman *villa rustica* complex with several individual buildings, associated with the local basalt quarries exploited for the Roman millstone industry, was detected and excavated (Grünewald, 2011, 2012; Totschnig & Seren, 2011). The area is characterized by intense agricultural land use and covers a slightly convex, southerly exposed slope inclining towards the east–west running Segbach (Figure 2a).

### 3 | METHODS

The subsurface gully structures investigated here were first detected during geophysical investigations of the Roman *villa rustica* site (northwest part of the Lungenkärchen site, Figure 2). As any detailed regional accounts on these structures were lacking at that time, the geophysical survey, in particular magnetometer prospecting, was extended and supplemented by pedo-sedimentary and geochronological investigations in order to characterize these relict landforms in detail, to assess the spatial extent and to verify their volcanic origin.

#### 3.1 | Geophysical prospecting

In the north-western part of the site, a magnetometer prospecting was carried out over an area of 43,395 m<sup>2</sup> by the Zentralanstalt für

Meteorologie und Geodynamik (ZAMG), Vienna, Austria. Measurements were carried out using a Förster FEREX Fluxgate 4-channel magnetometer in a grid of 0.16 m × 0.5 m. The measurements were triggered by wheel-based optical distance detection in steps of 0.16 m. The resolution of measurement was 0.1 nT and 20 measurements per second. A part of this area (23,729 m<sup>2</sup>) was prospected using georadar (Sensors & Software Noggin, PulseEKKO PRO) with 250 MHz antennas and a raster of 0.05 m × 0.5 m (Totschnig & Seren, 2011). The area to the east of the *villa rustica* was prospected by the ArchaeoGeophysics group at the University of Cologne using a Geometrics G-858 MagMapper Cs vapor magnetometer equipped with four sensors (50 cm distance). It operates at a range of 20,000 to 100,000 nT. The data was processed using Surfer 8 and MagMap 2000 software.

#### 3.2 | Field documentation and sampling of stratigraphic profiles

Soils and sedimentary deposits inside and around the gullies were investigated based on eight trenches (some of which perpendicularly cut the gullies at different parts of the slope), as well as 10 sediment cores (Figure 2). Trenches were dug using a small excavator. Sediment cores were retrieved by using an Atlas Copco Cobra mkII coring device and open steel auger heads, 6.0 and 5.0 cm in diameter, as well as closed ones operated with polyvinyl chloride (PVC) liners. The open cores were documented and sampled in the field. Trench profiles were drawn at a 1:10 or 1:20 scale. Soil texture, soil type and sedimentary texture were documented in the field using Ad-hoc AG Boden (2005) and the Munsell Soil Color Chart.

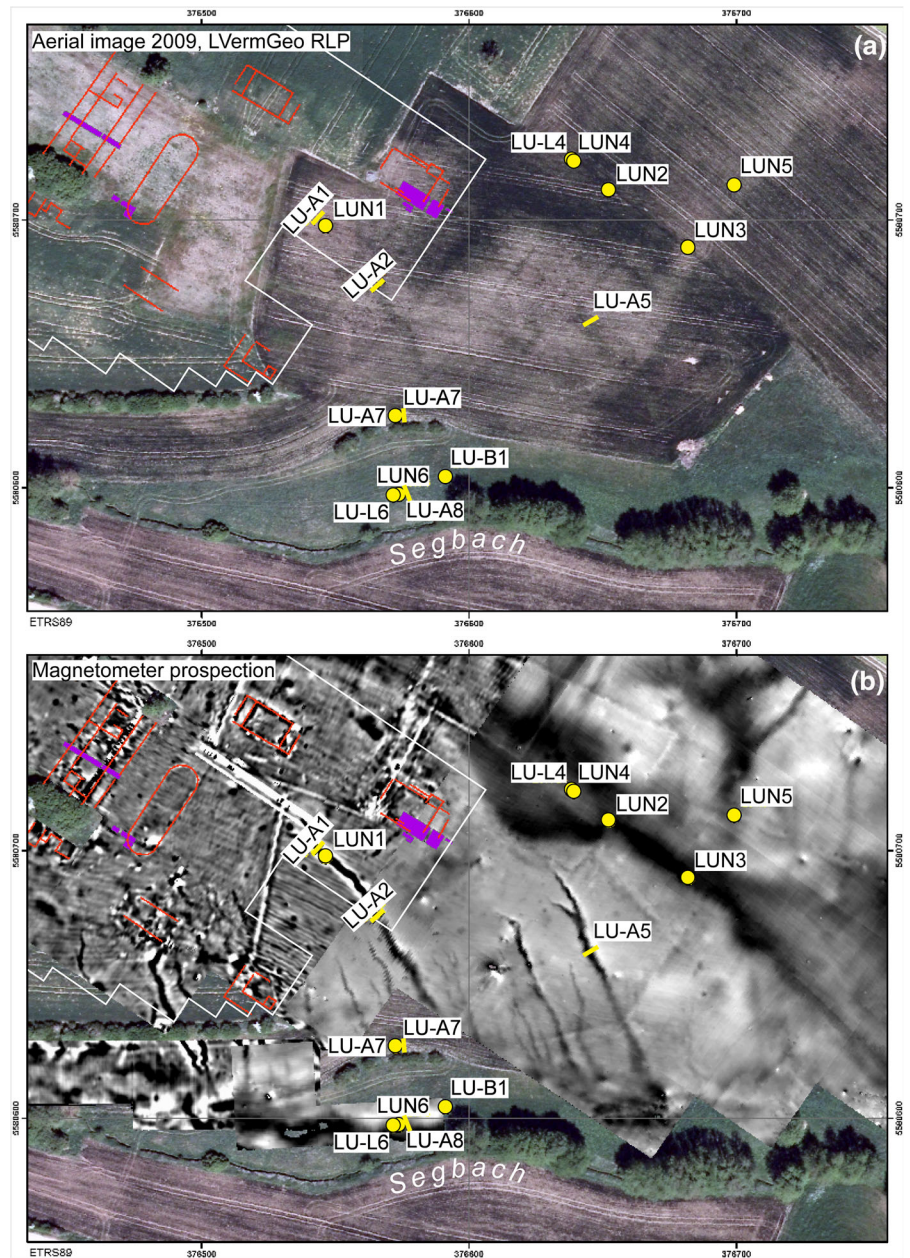
#### 3.3 | Grain size and lithological analyses

Selected units were sampled in plastic bags for pedo-sedimentary analyse at the Laboratories for Physical Geography at the Universities of Mainz and Cologne, Germany. Samples were air-dried, carefully hand-pestled and dry-sieved (2 mm). The fraction 0.063–2 mm was wet-sieved, whereas pipette analysis (Köhn, 1928) was used to determine the grain-size distribution < 0.063 mm. Samples for grain-size analysis were dried at 105°C before adding hydrogen peroxide (H<sub>2</sub>O<sub>2</sub>) (30%) to remove organic carbon. After dilution, (NaPO<sub>3</sub>)<sub>6</sub> and NaCO<sub>3</sub> were added for aggregate dispersion. Statistical parameters were calculated using GRADISTAT (Blott & Pye, 2001). For each sample from LU-A5, the ratio between the coarse siliciclastic (mainly schist, greywacke, quartzite) and tephra components > 2 mm was recorded.

#### 3.4 | Analysis of bulk density and saturated water conductivity

To compare the density and saturated water conductivity of the gully infill and the surrounding soils, undisturbed samples were taken from trench LU-A5 using 5 cm × 5 cm aluminum cylinders. A UMS KSAT device was used following the manual of UMS GmbH (2012); saturation of samples took between < 1 (sandy substrates) and 24 h (clay- and silt-rich substrates).

**FIGURE 2** Overview of the core study area “Lungenkärchen” (see white rectangle in Figure 1a for location). It shows the location of trenches (yellow bars) and sediment cores (yellow dots) as well as Roman archaeological structures (part of a villa rustica) deduced from the geophysical prospection (red lines) and archaeological excavations (purple signature) (for details on the archaeological structures see Grünewald, 2012). (a) Aerial image from 2009 provided by LVermGeo Rheinland-Pfalz showing some of the linear gullies through differential soil moisture. (b) Magnetometer prospection of the study area indicating the spatial distribution of the gullies oriented towards the Segbach running in a west–east direction. Coordinates represent UTM zone 32N



### 3.5 | Thin-section analysis

Two undisturbed samples from trench LU-A1 were taken for thin-section analyses using Kubiëna boxes (5 cm × 7 cm), one inside and one outside the channel structure. Samples were dried at 40°C for several days and impregnated using Oldopal P80-21, then cut and polished (final thickness = 30 µm) following Beckmann (1997). Flatbed scans of the thin sections were obtained at 1200 dpi and investigated at low magnification. Each thin section was scanned under ordinary light and using two polarization foils mounted above and below the thin section at an angle of 90°. Furthermore, the thin sections were inspected under plane polarized light (PPL), crossed polarizers (XPL), and oblique incident light (OIL) at magnifications of 12.5× to 500× using a polarization microscope (Axioskop 40, Zeiss). Micromorphological description followed the terminology of Stoops (2003), which includes a distinction between properties of pore space, groundmass, and pedofeatures. In general, the size, shape, and type of mineral and organic matter components were recorded and the nature of the pore space defined.

### 3.6 | Luminescence dating

At both study sites, samples were taken for optically stimulated luminescence (OSL) dating. While the four samples from trench LU-A1 and from core LU-L6 (Figure 2) at Lungenkärchen were dated in the luminescence laboratory of the Institute of Geography at Humboldt University of Berlin, Germany, the two samples later taken from the WBW were dated at the Cologne Luminescence Laboratory (CLL) of the Institute of Geography, University of Cologne, as the laboratory in Berlin had ceased operations shortly after processing the first batch. Therefore, slightly different protocols were applied for both sites.

For Lungenkärchen, the grain fraction between 63 and 250 µm was prepared applying standard laboratory procedures of the quartz coarse-grain method: wet sieving, removal of carbonates and organic material with hydrochloric acid (HCl) (10%) and H<sub>2</sub>O<sub>2</sub> (10%), mineral separation with heteropolytungstate (densities of 2.7, 2.62 and 2.58 g/cm<sup>3</sup>), and etching of the quartz fraction with hydrogen fluoride (HF) (40%) for 60 min. For quartz-OSL measurements, 1 mm- and 2 mm- aliquots were prepared. When signal efficiency was sufficient,

1 mm-aliquots were preferred to reduce the number of grains per aliquot in order to allow a better identification of the best-bleached grain population.

Equivalent doses ( $D_e$ ) were determined using a Risø TL-DA-15C/D reader equipped with a  $^{90}\text{Sr}/^{90}\text{Y}$  beta source delivering  $\sim 0.097$  Gy/s at the sample position. Sets of 18 to 45 aliquots per sample were stimulated with blue light emitting diodes (LEDs) ( $\lambda = 470 \pm 30$  nm) at  $125^\circ\text{C}$  for 40 s (Figure S2). The resulting OSL signals were detected in the near-ultraviolet (UV) range through a 7.5 mm Hoya U340 filter (transmission between 290 and 370 nm). For  $D_e$  determination, the initial integral of 0.48 s was used subtracting the last 4 s of the OSL decay curve. A standard single-aliquot regenerative (SAR) dose protocol following Murray and Wintle (2000) was used for OSL measurements, preheating at  $220$  or  $240^\circ\text{C}$  for 10 s and a test-dose cut-heat at  $160^\circ\text{C}$  (Supporting Information Table S1). The preheat temperatures were set after performing dose-recovery tests on sample LU-L6-185. The  $D_e$  distributions were analyzed using either the central age model (CAM) or, where poor bleaching is indicated through positively skewed and/or multimodal  $D_e$  distribution, the minimum age model (three-parametric MAM) after Galbraith et al. (1999) allowing for an overdispersion of  $\sigma_b = 0.1$  (Figure S3). This  $\sigma_b$  value was derived from dose-recovery test results, where an overdispersion of 9.3% was determined on bleached and laboratory-irradiated aliquots. Furthermore, the overdispersion of the  $D_e$  distribution of the well-bleached sample LU-A1-13 (10.8%) was a reference. Aliquots were selected for  $D_e$  calculation only if the recycling ratio was between 0.85 and 1.15 and the recuperation  $< 20\%$ .

The water content of the samples (relating to the dry weight) was determined after drying at  $105^\circ\text{C}$  for 24 h and an error of 5% was considered. High-resolution gamma spectrometry was applied to estimate the sediment dose rates arising from the decay of primordial radionuclides (Tables S2 and S3). The cosmic-dose rate was estimated considering the geographic position ( $50.5^\circ\text{N}$ ,  $7^\circ\text{E}$ ), the altitude (285 m) and half of the sampling depth. Luminescence ages were calculated using Adele software v2017 (Degering & Degering, 2020, <https://www.add-ideas.com>). In core LU-L6, the dose rate could not be determined directly from the layer of the OSL sample, but from the adjacent layers. To receive the dose rates for luminescence age determination of the samples of core LU-L6, layer models were calculated in Adele. All luminescence data of LU-A1 and LU-L6 are summarized in Tables 1 and S4.

At the WBW, one sample was collected from the gully infill (WBW-B), a second sample from the reworked loess and tephra deposits into which the gully had incised (WBW-A). Luminescence

signals of the quartz population were tested first, but they turned out to be relatively dim and decay-curve fitting with the R package 'Luminescence' version 0.9.0.88 (Kreutzer, 2019) indicated quartz signals not dominated by the fast component for more than 50% of the measured aliquots (Figure S4a). Furthermore, analysis of the signal curves in the Analyst software (Duller, 2015) showed that depletion ratios were inadequate ( $< 0.8$ ) for more than 50% of the measured aliquots as well (Figure S4b), indicating problems with feldspar contamination.

Therefore, ages were based on infrared stimulated luminescence (IRSL) dating of potassium feldspar (KF). KF grains in the  $100\text{--}200\ \mu\text{m}$  fraction were extracted by dry sieving, chemical treatment with HCl (10%) and  $\text{H}_2\text{O}_2$  (10%) to remove carbonates and organic matter, and density separation with sodium-polytungstate (KF  $< 2.58\ \text{g}/\text{cm}^3$ ). The feldspar extracts were measured on 2 mm-aliquots. The  $D_e$  measurements were performed on a Risø TL/OSL reader equipped with a  $^{90}\text{Sr}/^{90}\text{Y}$  beta source delivering  $\sim 0.15$  Gy/s at the sample position, infrared (IR) LEDs ( $\lambda = 870 \pm 40$  nm) and 5 mm blue D410/30x LOT interference filter ( $\lambda = 410 \pm 30$  nm). Measurements followed a feldspar SAR dose protocol (Wallinga et al., 2000) with preheat at  $270^\circ\text{C}$  for 60 s and IR signal stimulation at  $50^\circ\text{C}$  for 300 s (see Table S5). All dose-response curves were forced through the origin. Protocol performance for the WBW samples was tested using a preheat-plateau experiment with preheat temperatures between  $210$  and  $290^\circ\text{C}$  (doses are independent from thermal pre-treatment for temperatures of  $230$  to  $290^\circ\text{C}$ , Figure S5), as well as dose-recovery experiments with laboratory doses of  $\sim 50$  Gy administered after bleaching in a Hönle Sol2 solar simulator for 24 h (mean dose-recovery ratios of  $1.00 \pm 0.05$  for WBW-A and  $0.99 \pm 0.03$  for WBW-B;  $N = 5$ ). The signals for  $D_e$  determination were derived by subtracting a background estimated from the last 60 s of the decay curve from the first 18 s of the decay curve.

The  $D_e$  distributions of both samples are plotted in Figure S6. Since asymmetric dose distributions and significant dose scatter with overdispersion values  $> 30\%$  (calculated using the CAM; Galbraith et al., 1999) point to incomplete bleaching of the samples, burial doses were calculated with the bootstrapped version of the three-component MAM<sub>bs</sub> (Cunningham & Wallinga, 2012) using an empirical  $\sigma_b$  of  $0.15 \pm 0.10$  (Figure S6). Luminescence ages were calculated with the DRAC software version 1.2 (Durcan et al., 2015) by combining MAM<sub>bs</sub>-derived burial doses, uranium (U), thorium (Th) and potassium (K) concentrations of the sediment derived from high-resolution gamma spectrometry (using the conversion factors of Guerin et al. [2011]), water contents of  $20 \pm 5\%$  (rounded based on oven-drying of samples at  $50^\circ\text{C}$ ), internal K contents of  $12.5 \pm 0.5\%$

**TABLE 1** Parameters used in optically stimulated luminescence (OSL) age calculation for LU-A1 and LU-L6 at Lungenkärchen

OSL sample (lab ID)	Depth (m b.s.)	DR (Gy/ka)	N	OD (%)	Skewness	Dose (Gy)	Grain size ( $\mu\text{m}$ )	Aliquot size (mm)	Age (ka) [age model]
LU-A1-13 (HUB-0179)	0.9	$4.62 \pm 0.22$	14/18	10.8	0.45	$60.21 \pm 2.31$	63–90	2	$13.0 \pm 0.3$ [CAM]
LU-L6-120 (HUB-0301)	1.2	$3.51 \pm 0.2$	14/18	28.0	1.06	$6.17 \pm 0.66$	90–250	1	$1.8 \pm 0.2$ [MAM ( $\sigma_b = 0.1$ )]
LU-L6-185 (HUB-0302)	1.85	$3.11 \pm 0.23$	34/45	19.8	1.08	$44.42 \pm 2.77$	63–250	1; 2	$14.3 \pm 1.0$ [MAM ( $\sigma_b = 0.1$ )]
LU-L6-270 (HUB-0304)	2.7	$3.68 \pm 0.46$	16/22	40.0	1.22	$51.48 \pm 6.39$	63–250	2	$14.0 \pm 1.8$ [MAM ( $\sigma_b = 0.1$ )]

Note: DR = total dose rate; N = number of aliquots (selected/measured); OD = overdispersion; grain size = measured grain-size fraction; CAM = central age model; MAM = minimum age model, along with final ages. For dose-rate measurements see Supporting Information Table S4

(Huntley & Baril, 1997) and  $a$ -values of  $0.07 \pm 0.02$  (Kreutzer et al., 2014). The samples showed no indication of significant disequilibria in the Th and U decay chains (Table S6). Ages were corrected for anomalous fading following the approach of Huntley and Lamothe (2001) and experimental  $g_{2\text{day}}$ -values (using delay times of up to 6 h and the approach according to Auclair et al. [2003]) of  $4.0 \pm 0.5$  and  $3.7 \pm 0.8\%$ /decade for WBW-A and WBW-B, respectively ( $g$ -values are the arithmetic mean of five aliquots) (Figure S7). The luminescence data for both samples are summarized in Tables 2 and S7.

### 3.7 | Radiocarbon dating

Four charcoal samples were dated by carbon-14 ( $^{14}\text{C}$ )-accelerator mass spectrometry (AMS) at the Institute of Geology and Mineralogy, University of Cologne. The data were calibrated using Calib 7.1 (Stuiver & Reimer, 1993) and the IntCal13 database (Reimer et al., 2013). All data are reported as cal BP using the  $2\sigma$  confidence interval (Table 3).

## 4 | RESULTS

### 4.1 | Lungenkärchen

#### 4.1.1 | Geophysical prospection

The magnetometer prospection near the *villa rustica* as well as the slope towards the bottom of the Segbach Valley reveals linear, roughly isohypse-perpendicular anomalies up to 4 m wide (Figure 2). Besides the five well-identified larger structures, there are several shorter, more narrow ones, which are very closely spaced (less than 10 m). The larger ones initiate further up the slope and tend to bifurcate. The downslope termination of the linear anomalies is hardly visible in the composite magnetometer image. The same structures are clearly visible in the ground-penetrating radar (GPR) depth slices at 0.4–0.8 m down to 2.0–2.4 m below the surface (Figures 3 and S8).

### 4.1.2 | Stratigraphic evidence

#### Trench LU-A1

Trench LU-A1 (Figure 4) cuts the V-shaped gully structure of the most prominent linear anomaly (Figure 2b), which has a width of c. 2.7 m and a depth of c. 1.5 m. The boundary of the gully (Layers 11–13) is clearly visible and it is incised into stratified tephra-dominated deposits of varying thickness and particle-size distribution (Layers 5–10). Layers 5–8 are relatively fine-grained with clay- and silt-sized particles accounting for roughly 50%. Only Layer 5 shows a significant lapilli component. Layers 9 and 10 are dominated by lapilli and sand-sized particles. The thin section from Layer 8 in Figure 4 shows a sequence of five finely stratified and densely packed layers with low to medium porosity (Figure 5a, c). Pores mainly classify as simple

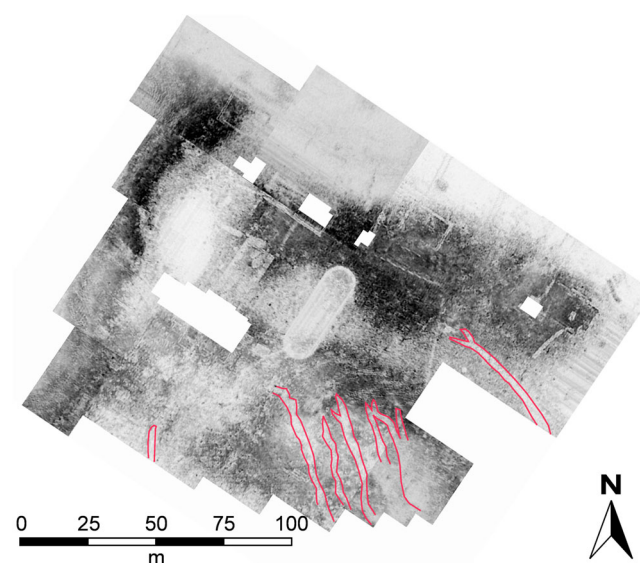


**FIGURE 3** GPR depth slice of the area around the Roman villa at “Lungenkärchen”, showing a depth range of 1.6 to 2.0 m below surface (location on Figure 2 is indicated by the white line). The proximal, upslope parts of the linear channels in the southern part of the prospected area running toward the Segbach Valley bottom are clearly visible (marked by red lines). Figure S8 shows a selection of several depth slices of the site

**TABLE 2** Summary of luminescence data for samples WBW-A and WBW-B

Sample	Depth (m b.s.)	DR (Gy/ka)	N	OD (%)	Dose (Gy)	Grain size ( $\mu\text{m}$ )	Aliquot size (mm)	Age <sub>unc</sub> (ka)	g-Value (%/decade)	Age <sub>cor</sub> (ka)
WBW-A	2.6	$4.4 \pm 0.3$	20	$61 \pm 10$	$29.6 \pm 6.7^*$	100–200	2	$6.7 \pm 1.6$	$4.0 \pm 0.5$	$9.7 \pm 2.5$
WBW-B	2.4	$4.5 \pm 0.3$	49	$57 \pm 6$	$29.9 \pm 12.3$	100–200	2	$6.7 \pm 2.8$	$3.7 \pm 0.8$	$9.4 \pm 4.1$

Note: WBW = Wingertsbergwand; U = uranium; Th = thorium; K = potassium; DR = total dose rate; N = number of measured and accepted aliquots; OD = overdispersion derived by the central age model; Age<sub>unc</sub> = uncorrected infrared stimulated luminescence (IRSL) age; Age<sub>cor</sub> = fading-corrected IRSL age.

**TABLE 3** Results of carbon-14 ( $^{14}\text{C}$ )-accelerator mass spectrometry (AMS)-dating

Sample	Lab-ID col #	Material	$^{14}\text{C}$ age BP	$\delta^{13}\text{C}$	cal BP ( $2\sigma$ )	rp (%)
LU-A3-4a-HK1	2628.1.1	Charcoal ( <i>Fagus</i> sp.)	$1865 \pm 35$	−24.1	1878–1716	100.0
LU-A5-5-HK1	2629.1.1	Charcoal ( <i>Quercus</i> sp.)	$2138 \pm 34$	−26.4	2163–2003, 179–2167, 2302–2243	78.5, 1.8, 19.7
LU-A8-3-HK1	2630.1.2	Charcoal ( <i>Quercus</i> sp.)	$1596 \pm 33$	−29.5	1552–1408	100.0
LU-L6-140	1463.1.1	Charcoal (indetermined)	$3519 \pm 32$	−27.7	3879–3700	100.0

Note: rp = relative area under probability distribution.

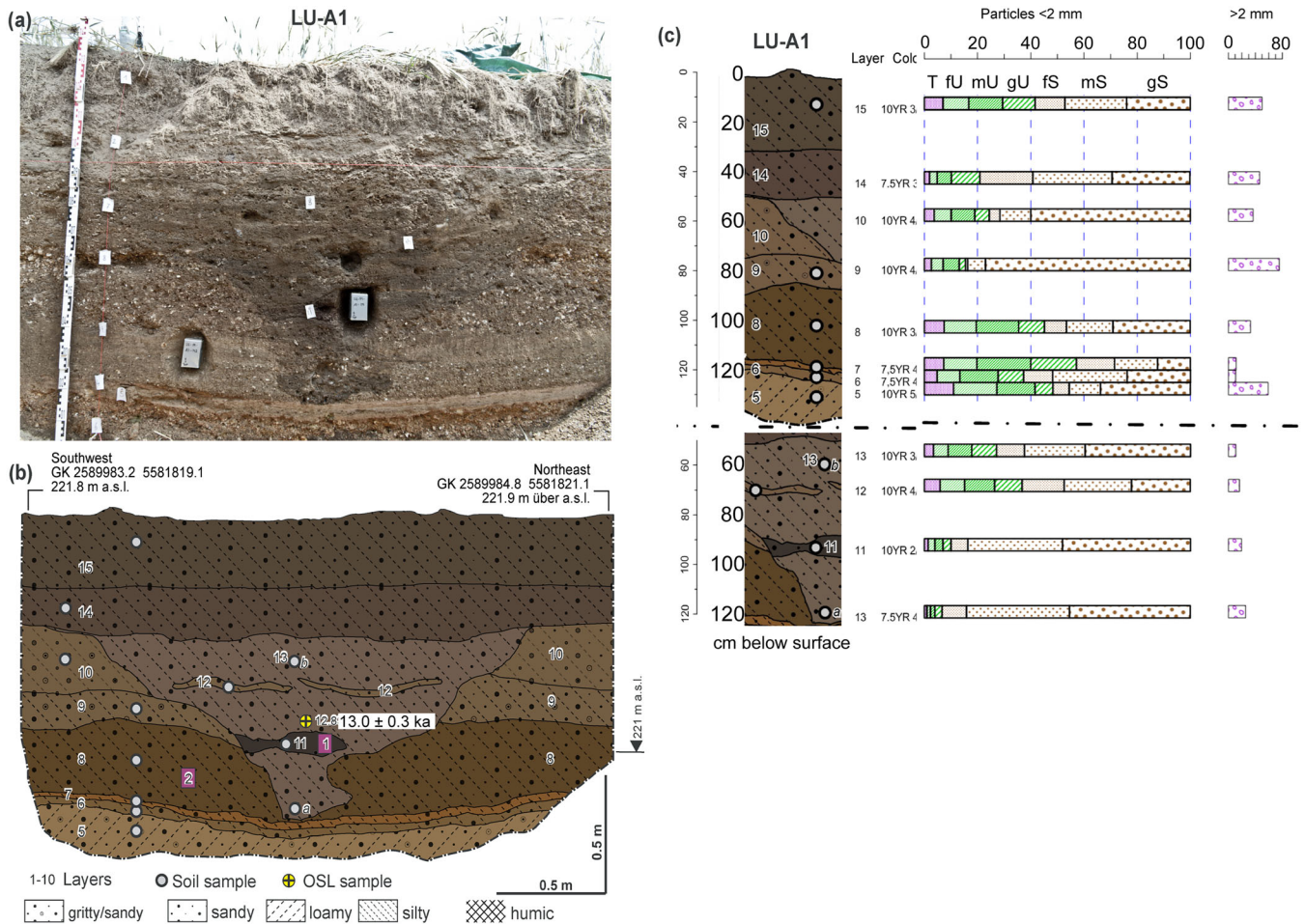


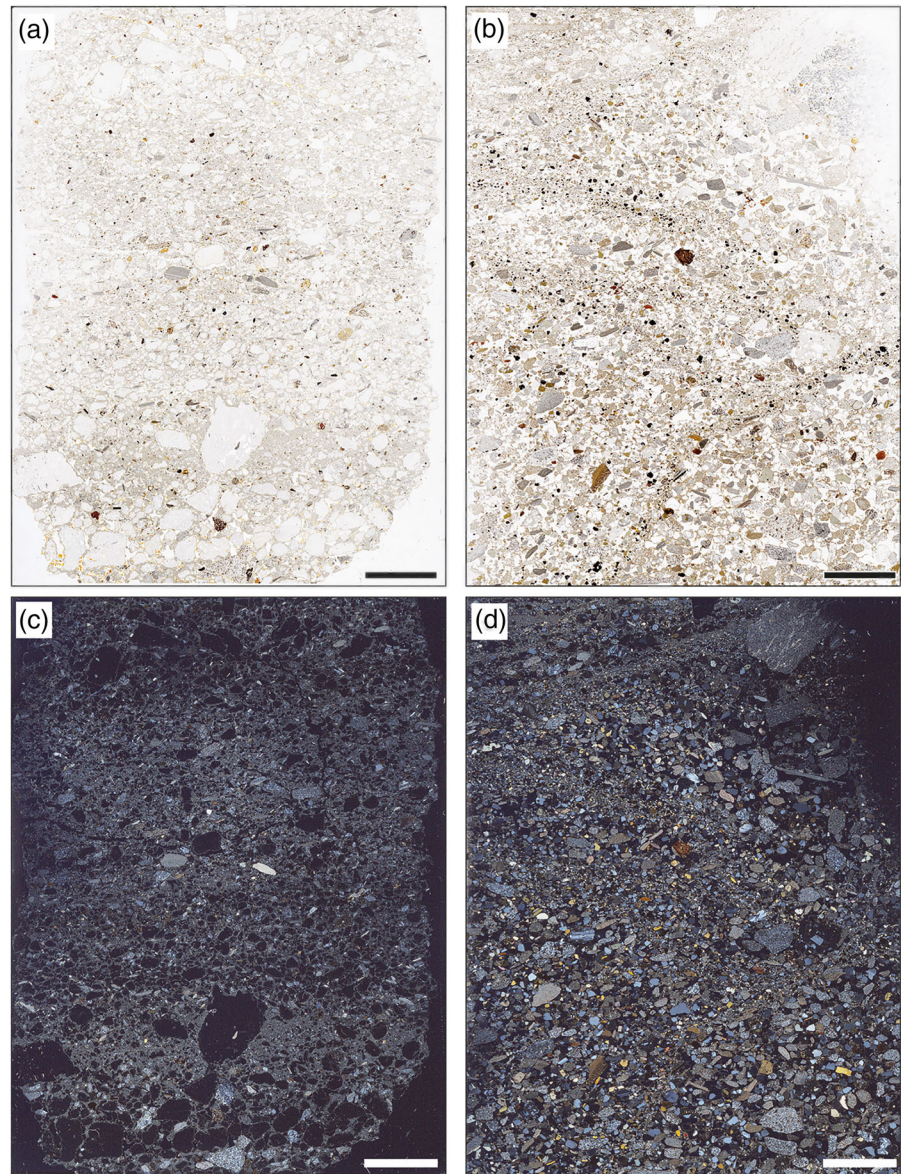
**FIGURE 4** Trench LU-A1 showing the proximal part of one of the most prominent gullies running towards the Segbach, including photograph (a) and drawing (b) of the trench wall (purple boxes = samples for thin sections). Panel (c) shows the different layers with Munsell colour codes, particle-size distribution (T = clay, fU = fine silt, mU = medium silt, gU = coarse silt, fS = fine sand, mS = medium sand, gS = coarse sand) and the percentage of particles > 2 mm. For location see Figure 2

packing voids, vugs and a few irregular planes. Organic matter was not found. The groundmass is composed of varying amounts of either subangular to rounded light gray to gray rock fragments and mineral grains ranging from silt to medium grit, indicating polymodal size distributions and reflecting the grain-size distribution data (Figure 4c). Most of the clast components are highly porous and consist of isotropic matter due to their pyroclastic origin. Furthermore, siltstone and quartzite particles, as well as a few iron oxide-rich opaque grains can be identified. The finer size fraction comprises elongated grains, mostly feldspar crystals and other siliciclastic rock particles. The micromass (submicroscopic grains > 5 μm in diameter) has a grey colour and turns black under crossed polarizers indicating that at least a part of it is composed of volcanic fines or isotropic weathering products such as allophanes. Few orange, mostly limpid and partly impure and/or microlaminated coatings of illuvial clay are present, with a maximum size of c. 200 μm. The coatings show no or light grey interference colours, and weak to no primary fluorescence. They probably consist of allophane (no birefringence), hallyosite or kaolinite (weak birefringence) as reported for clay coatings in soils derived from LST elsewhere (Poetsch & Altemüller, 1990). No further pedogenetic features are present.

The gully infill (Layers 11–13) is dominated by silt to sand-sized particles in the upper part and sand- to grit-sized particles in the lower part, which is very narrow and develops a notch along the north-

eastern margin. A quartz-OSL sample from the center of the gully infill was dated to 13.0 ± 0.3 ka (LU-A1-13). The luminescence properties of this sample were satisfactory, implying sufficient OSL signal intensity as well as well-shaped OSL shine-down and dose–response curves, and no  $D_e$  outliers were observed. The only slightly positively skewed  $D_e$  distribution was analyzed with the CAM (Galbraith et al., 1999). Stratification is not as clear as in the laterally confining facies and appears more undulating (see Layer 12). A thin section from Layer 11 (Figure 5b, d) confirms this, revealing a lack of clear separation into parallel layers. However, some preferential accumulation of opaque grains along inclined planes is visible, which indicates incomplete mixing of the deposit. Locally, graded bedding is present. The pore space is dominated by simple packing voids and porosity is medium to high. The thin section contains less lapilli and more fragments of siltstone and quartzite compared to Layer 8 and is overall dominated by medium to coarse sand and fine grit. The lower amount of silt- and clay-sized particles confirms the grain-size distribution data (Figure 4c). Fine grains tend to be attached to larger grains and have textural coatings, while outside of the channel infill, in Layer 8, the larger grains float in the fine groundmass. Many crystals of feldspar and few mica grains are present. Furthermore, opaque sand grains are more abundant, while the orange clay coatings are missing. Finally, aggregates of finely graded lamination were found in the upper part of the thin section. These are interpreted as fragments of

**FIGURE 5** Flatbed scans of thin sections LU-A1-M2 (a) and LU-A1-M1 (b) from trench LU-A1 (Figure 4). Panels (c) and (d) show the same thin sections scanned with two polarization foils. Scale bars are 10 mm long



depositional surface crusts which can be formed by raindrop impact and overland flow (Pagliai & Stoops, 2010). No pedogenetic features were observed.

The gully infill is overlain by *c.* 50 cm of poorly sorted upper soil (Layers 14 and 15), with a plough horizon of *c.* 30 cm (Layer 15) characterized by a higher concentration of organic matter. In the north-eastern part of the study area, the uppermost plough horizon contains *c.* 6% of organic matter (cores LUN2, LUN4 in Figure 2) based on loss-of-ignition measurements, compared to stable values around 4% in the layers below (Hüls, 2012). The poorly sorted texture comprises clay to grit components (Figure 4c).

#### *Trench LU-A5*

Trench LU-A5 shows a *c.* 7.5 m wide and 1.5 m deep channel, separated into six different layers (Figure 6). Layer 1 represents the pre-incision, horizontally laminated LST deposits with a high concentration of lapilli. It has a low density around 1 g/cm<sup>3</sup> that correlates with a relatively high saturated water conductivity. The amount of non-tephra coarse components is *c.* 40% on average. The channel infill (Layers 2–4) is also dominated by sand-sized to grit-sized components. At the base of the wide, V-shaped structure the siliciclastic

components reach almost 70–80%, but their concentration reduces upwards and they almost disappear in Layers 3 and 4, with the exception of sediment lense 4a. Its bulk density (1.4–1.7 g/cm<sup>3</sup>) is higher compared to the surrounding tephra and correlates with lower saturated water conductivity, particularly in the upper, tephra-dominated part (Layer 4). In the southwest, the channel infill (Layer 3) is laterally confined by Layer 5, which is structureless and has a higher amount of non-volcanic components. The remarkably young <sup>14</sup>C age of a charcoal piece of 2243–2163 cal BP, the cluster of charred oak-wood fragments identified in the exposure and the presence of La Tène-age artifacts (*c.* 450 BCE to the turn of eras; *c.* 2400–1950 on the cal BP scale) at other trenches of the study site (e.g., LU-A8, Figure 7) and as stray finds (Grünwald, 2011, 2012), point to an anthropogenic infill; possibly a La Tène-age pit of a wooden post, disintegrated into charred oak wood. Layer 6 represents the recent agricultural soil overlying the incised channel structure.

#### *Further trenches*

Trench LU-A8 represents the proximal part of a terminal fan connected to the gully of LU-A1 (Figures 2 and 7). Both OSL and <sup>14</sup>C data clearly show a hiatus at *c.* 1.65 m below surface between the terminal



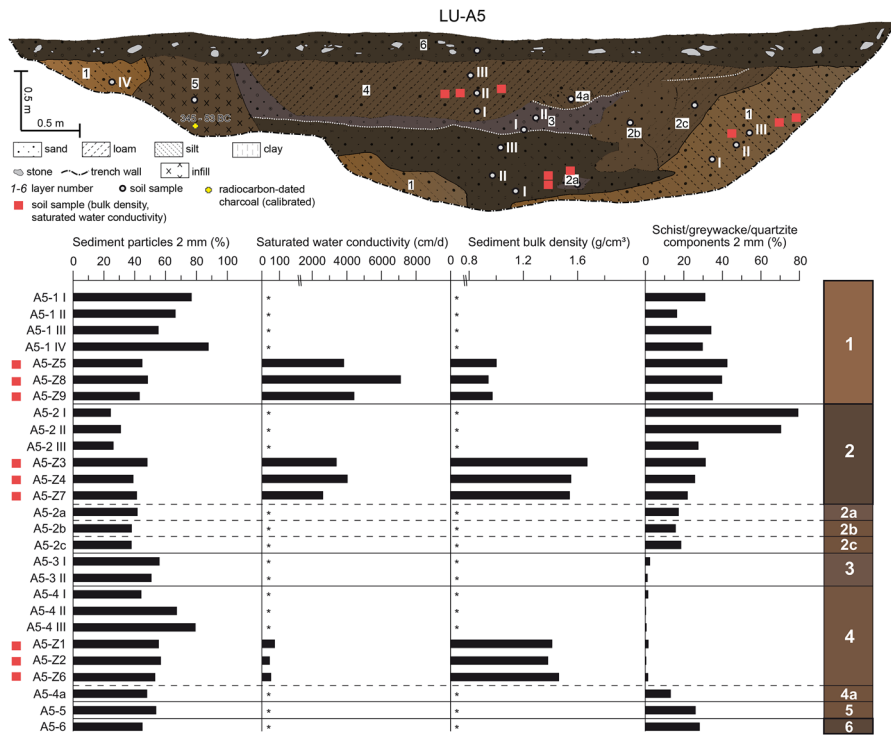


**FIGURE 6** Trench LU-A5 representing the upper to middle part of the easternmost prominent channel running in south-eastern direction. A sketch of the trench is shown, with labeled samples analyzed for the coarse fraction > 2 mm, saturated water conductivity, sediment bulk density (\* = no measurement), and the amount of non-volcanic particles among coarse components. For location of LU-A5 see Figure 2

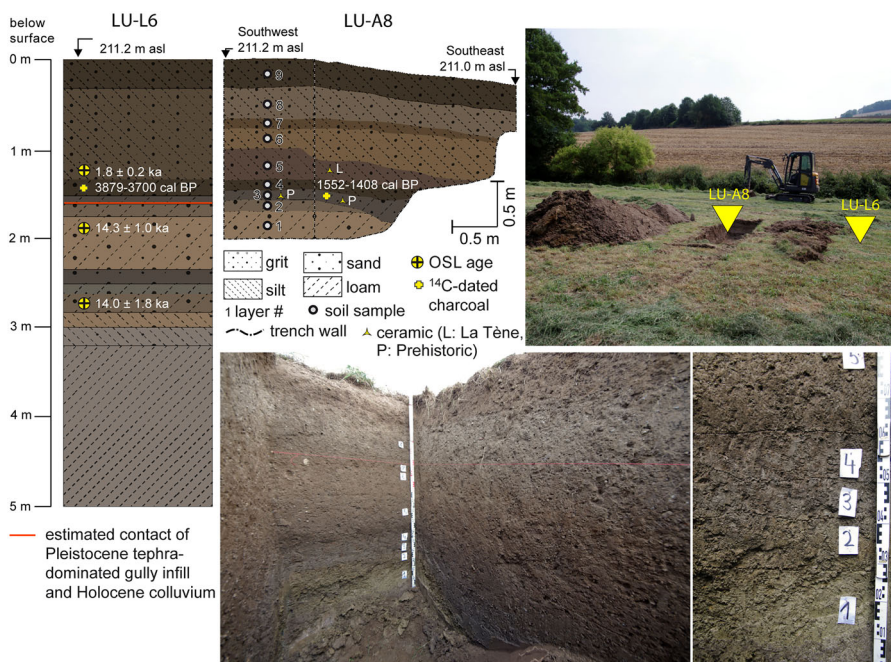


**FIGURE 7** Trench LU-A8 and parallel core LU-L6 (see also Supporting Information Figure S9) representing the proximal part of the terminal fan of one of the most prominent gullies running towards the Segbach Valley. For location see Figure 2

fan deposits, which are dominated by lapilli and connected to the channel infill (OSL: 14.0 ± 1.8 ka, 14.3 ± 1.0 ka), and the overlying coluvial deposits (<sup>14</sup>C: 3879–3700 cal BP, 1552–1408 cal BP; OSL: 1.8 ± 0.2 ka) (Figures 7 and S9; Tables 1 and 3), which also contain Prehistoric artifacts, some more precisely dated to the La Tène age (Grünewald, 2012), as well as many charcoal fragments. The dark and humic Layer 4, that contains both <sup>14</sup>C data reported earlier, may represent a fossil A-horizon, that is a temporarily stable surface. At the base of the third meter of core LU-L6 (right next to LU-A8), a bright band of well-stratified, pure volcanic ash was found (Figures 7 and S9). In contrast to the OSL dating of trench LU-A1, the luminescence properties were less suitable here, while water contents were very high in the two lower samples, which were taken at and below the

groundwater table. Many aliquots showed a slow decay of the OSL signal (although no feldspar contamination) or increased recuperation. Accordingly, many aliquots had to be excluded from further analysis (Table 1). Overall, the finer-grained sand showed better luminescence properties compared to the coarser fractions. The resulting positively skewed dose distributions with overdispersion values of up to 40% indicating poor bleaching were evaluated with the MAM (cf. Galbraith et al., 1999) (Figure S3; Table 1).

Trench LU-A2 (Figure S10), c. 50 m downslope of LU-A1 (Figure 4), not only cuts the LST sequence and a thin late Pleistocene cover bed, but also reaches the uppermost part of the Lower Miocene clays and silts at a depth of c. 1.5 m below surface. It is c. 5 m wide and 1.7 m deep. The gully base shows distinct, dark iron (Fe) and

manganese (Mn) precipitation and strongly contrasts with the underlying light clays and silts (Figure S11).

## 4.2 | Wingertsbergwand

For chronological confirmation and correlation of the gullies at Lungenkärchen south of Mendig with other, previously known LSE-related channel structures (cf. Schmincke, 2014), we attempted to generate OSL data from the WBW site, where the ULST is cut by several similar channels in the uppermost part of the wall (Figure 8b). However, the only accessible site at the time of sampling, was the gully WBW-A1. It contains silt-rich deposits and tephra and is cut into an alternating, horizontally bedded sequence of light yellowish brown silts and tephra in varying ratios. Stratigraphically overlying the ULST, the tephra component stems from reworked upslope ULST deposits, while the silt component may be derived from earlier, late Pleistocene sedimentation of loess (cf. Schmincke, 2014) or dust accumulation during the Younger Dryas. Both substrates are proximally dislocated and slightly mixed, suggesting solifluctional transport. The gully is c. 4 m wide and 2 m deep. The upper part of the gully infill is decalcified, whereas along the boundary of the incision carbonates have reprecipitated (Figure 8a). While the gully deposits were IRSL-dated to  $9.4 \pm 4.1$  ka, the incised pre-incision strata were IRSL-dated to  $9.7 \pm 2.5$  ka (Table 2). Similar to Lungenkärchen, asymmetric dose distributions, indicating incomplete bleaching, led to the application of the  $MAM_{bs}$  (bootstrapped MAM).

## 5 | DISCUSSION

Investigations from this study reveal the characteristics and spatial distribution of the gullies, as well as their genetic relationship to the LSE. The interpretation of the short, linear gullies identified in the magnetograms and GPR depth slices (Figures 2, 3 and S8) leading from the margins of the small plateau of the Roman *villa rustica* into the Segbach Valley was ground-truthed by the trenches cross-cutting the gullies. Although the pre-incision strata and the gully infill share common sediment sources (i.e., LST, pre-LSE soil, clastic components of local underlying schists, greywacke and quartzite), both units are significantly different in terms of colour, bulk sediment density, water conductivity, micro-lamination, and ratio of volcanoclastic to

siliciclastic components. Even though graded bedding is only weakly expressed in the thin section of the channel infill, when combined with the visible layering and surface exposure (i.e., textural crust), it is clearly indicative of transport by water; in contrast to solifluctional dynamics outside the gullies. Each graded sequence potentially relates to a specific discharge event (Vanwallegheem et al., 2005; Bork et al., 2006b). The bow-like shape of the accumulations of opaque grains may point to later movement by gravity microsides inside the gullies. Less distinct macro-scale bedding of the channel infill when compared to the outer tephra has also been observed in the few documented gullies of the more proximal tephra exposures in the Mendig Graben, that unequivocally formed during the LSE (Schmincke, 2014).

The Plinian eruption of the LSV – with several short phreatomagmatic interruptions in between – has induced the most significant changes in the wider study area during recent geological times. This is exemplified by the thick, slightly reworked tephra layers on top of the late Pleistocene solifluction layers, and the Miocene clay-silt deposits in the trench profiles. The eruption released an extremely hot gas column and large amounts of volcanic aerosols into the atmosphere, with immediate effects on solar radiation flows and cloud condensation in the lower atmosphere, inevitably resulting in thunderstorms with heavy downpours (Schmincke et al., 1999; Litt et al., 2003; Schmincke, 2014). Subsequently, even if only moderately strong rainfall was assumed, substantial surface discharge would have formed on top of the fresh, marginally permeable fine-grained ash deposits (cf. Collins et al., 1983; Major & Yamakoshi, 2005; Manville et al., 2009), leading to rapid formation of these gullies. By considering the  $1\sigma$  error ranges, the OSL data obtained from the gully infill (LU-A1) and the proximal part of the terminal fan (LU-L6) overlap with or come close to the LSE, and support the hypothesis of late-syn- and immediate post-eruptive formation and rapid gully infilling within a matter of years.

The May 18, 1980 Plinian eruption of Mount St Helens (Washington State, USA) provides crucial insights into how gully formation may have unfolded close to the LSV. There, the mainly silty airfall covering surrounding hillslopes – analogous to the tephra material that characterizes the proximal ULST facies near the LSV at Mendig (Schmincke et al., 1999) – revealed an infiltration capacity of 2 to 5 mm/h only (Collins et al., 1983). Erosion of loose tephra on these hillslopes occurred in the form of linear erosion, in some places even cutting down into the colluvium. A clear linear relationship

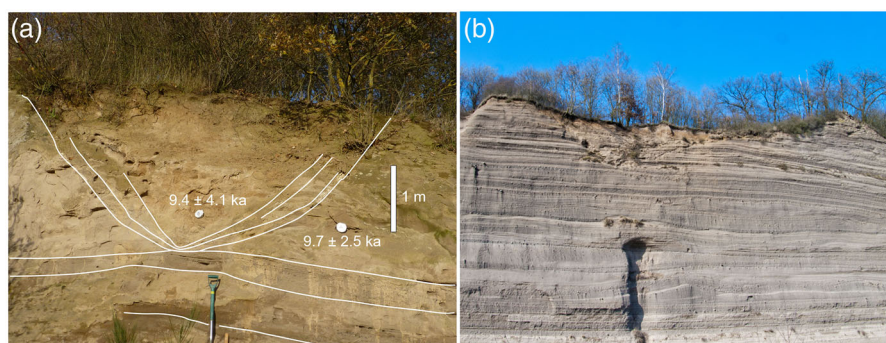


**FIGURE 8** (a) Channel structure in the uppermost part of the western Wingertsbergwand (reworked LST), sampled for OSL dating (see details in Table 2). It is incised into horizontally bedded silt and tephra deposits that stratigraphically overlie the ULST (not captured by the profile photograph). (b) Similar channel structures can be observed in other parts of the Wingertsbergwand, cut into the stratigraphically older ULST). In contrast to profile WBW-A1 in (a), these date syn- and immediately post-LSE (see also Schmincke, 2014)

between hillslope gradient and erosion rate was documented (Collins et al., 1983). This relationship may be extrapolated to the study site of Lungenkärchen when affected by the LSE. High surface discharge and erosional intensities can be deduced from the incision through the tephra layer into the late Pleistocene solifluction layer and even the clay-rich Miocene deposits, as shown in LU-A2 (Figures S10 and S11), and finally, also from the upslope end of the gullies reaching very close to the watershed.

The post-eruptive tephra incision and infill around Mount St Helens may qualify this site a modern analog for the subsurface gullies discovered at Lungenkärchen, which were formed by the LSE. Both eruptions were mainly Plinian with the widespread environmental effect of tephra deposition and the emission of rainfall-stimulating condensation nuclei, both inevitable for the formation of the type of gullies discussed here. A long-term monitoring study of erosion and hillslope change after the Mount St Helens eruption found dense rill and gully networks up to the size found at Lungenkärchen only a few weeks post-eruption. In August 1983, the edges of rills and gullies had been already smoothed and some of the larger rills had partially been filled with sediment derived from denudational processes. However, by October 2010, 30 years after the event, even the largest gullies had been entirely filled (Figure S12) (Collins & Dunne, 2019). Similar observations were made from a mainly phreatomagmatic eruption on Ambrym Island, Vanuatu, in 1913, where the formation of gullies of similar dimension as at Lungenkärchen is attributed to heavy rainfalls over a period of only days up to a few weeks after the event (Németh & Cronin, 2007). Likewise, gullying in fresh tephra deposits was the predominant erosional process at Mount Usu, Hokkaido, Japan, during the 1977–1978 volcanic activity phase. Some gullies cut down into the pre-deposition soils and reached up to 10 m in width and 5 m in depth (Chinen & Rivière, 1989, 1990).

Given the well-preserved nature of the edges of the gullies within the trench profiles at Lungenkärchen, it seems that they were filled very quickly, probably at a timescale similar to the Mount St Helens analog (Figure S12). In one of the very few literature accounts on gullies incised into the ULST deposits, Schmincke (2014, in Abb. 127) presents a V-shaped gully deeper and wider than those identified at Lungenkärchen in combination with syn-eruptive normal faulting adjacent to the WBW, that is closer to the LSV. At that site, a 25 cm-thick layer of primary fallout ashes within the gully infill is indicative of gully formation after violent rainfall which occurred before the end of the eruption (Schmincke, 2014); such syn-eruptive gully formation has also been inferred on Vanuatu (Németh & Cronin, 2007). The lowermost laminated pure ash deposit in the third meter of core LU-L6 (Figures 7 and S9) could be interpreted as primary fallout ash (*sensu* Schmincke, 2014) and, thus, may also indicate a syn-eruptive start of gully formation at the Lungenkärchen site.

Along the western part of the Lungenkärchen site, the spacing of the gullies is very narrow, in places even < 10 m (Figures 2 and 3), which is less than reported for the larger, more proximal gullies around the WBW; their spacing is 25–50 m (Schmincke, 2014). This positive relationship between channel size and spacing, however, is similar to other fluvial channel networks (according to the catchment-scale concept of stream orders, e.g., Strahler, 1957), and can be inferred for the post-eruptive gully network at Mount St Helens, too (Figure S12) (Collins & Dunne, 2019).

From another perspective, the fluvial infill of the gullies results in a higher bulk density and lower saturated water conductivity, which adds to heterogeneous pedo-sedimentary characteristics at the agricultural field scale (see e.g., differential moisture patterns visible in satellite imagery of Figure 2a). These pedo-sedimentary differences may lead to heterogeneous plant growth, crop yields and demands in fertilization, irrigation and pesticide application (Patzold et al., 2008), particularly where the overlying soil horizons are relatively thin. The impact of infilled gullies on agricultural production may be very significant at the field-scale, for example with a reduction of crop yields of up to 100% in a modern, artificially filled gully in the black soil region of northeast China (Liu et al., 2013). However, it remains to be tested if such findings can be transferred to the relatively dense pattern of fossil, much older volcanic gullies adjacent to the LSV and elsewhere. In contrast to infilled gully structures on agricultural land that are prone to the adverse effects of re-incision and that may show histories of multiple incision-and-infill cycles on decadal to centennial time-scales (e.g., Vanwalleghem et al., 2005), those related to the LSE are protected by several decimeters of overlying brown earths and regosols.

At the WBW, the IRSL date of post-LSE stratified silt and tephra deposits corroborates the interpretation of reworking mainly during the Younger Dryas and/or the early Preboreal. The poor bleaching and dim luminescence properties result in relatively large error ranges of 26% and 44%, respectively. Nevertheless, the stratigraphically younger infill of the gully ( $9.4 \pm 4.1$  ka) and the stratified silt and tephra deposits ( $9.7 \pm 2.5$  ka) reveal very similar ages. Therefore, it seems likely that incision and infill of this unit occurred soon after deposition of the reworked LST and loess during the terminal Younger Dryas or the early Holocene. The error ranges of the OSL data give way to two possible interpretations:

- i. The proximally reworked loess with tephra components dated to  $9.7 \pm 2.5$  ka was deposited during and subsequent to the late Younger Dryas, a time with reported aeolian deposition (Janotta et al., 1997; Dotterweich et al., 2013) and enhanced fluvial activity (e.g., Andres et al., 2001). Gully incision occurred under periglacial climate conditions with sparse vegetation cover and substantial generation of runoff (Lang & Mauz, 2006; Kaiser et al., 2007). These factors may have prevailed until the beginning of the Holocene as suggested by Dotterweich et al. (2013).
- ii. Gully incision was caused by cutting back from the outlet during the Preboreal (cf. Larsen et al., 2013), that is linear incision during the transition towards warmer temperatures, denser vegetation cover, and more stable hillslopes. This scenario would be supported by the youngest part of the OSL age range of  $9.4 \pm 4.1$  ka from the gully infill cut into the reworked loess and tephra of the WBW.

## 6 | CONCLUSIONS

Geophysical prospection of the archaeological site of Lungenkärchen south of the LSV shows distinct, short and in some parts closely-spaced parallel gullies (c. 10 m apart), with varying cross-profiles and a depth of up to 2 m. Pedo-sedimentary analyses clearly contrast the gully infill with the surrounding mixed soil and tephra. Both, the gully

infill and the surrounding facies consist of a mixture of siliciclastic and tephra components, while the infill shows a higher bulk density, lower saturated water conductivity, and a lower percentage of clay and silt fractions. The gully infill may – as in Layers 3 and 4 in LU-A5 – even entirely consist of tephra material. The surrounding facies appears macroscopically layered. The gully infill, however, only shows some graded bedding at the micro-scale in the micromorphological record, possibly relating to single discharge and infill events. OSL data from the gully infill range from  $14.0 \pm 1.8$  ka right at the base of the tephra-bearing units at the transition of the main gully and its terminal fan towards the valley bottom to  $13.0 \pm 0.3$  ka in the upper part of the same gully. All chronological data overlap with or come very close to the LSE, respectively.

At the recent candidate analog of Mount St Helens, the syn- and post-eruptive gully formation and their subsequent infill within just 30 years after the violent Plinian eruption of May 18, 1980, support the interpretation of rapid gully incision into LSE tephra layers in the study area during the end of and immediately after the LSE. Thus, findings made here on edaphic differences between the gully infill and surrounding soils may be relevant for similar areas characterized by tephra-dominated volcanic provinces at a global scale.

As the post-LSE deposits of the lateral WBW demonstrate, gully formation also occurred later, most likely during the terminal Younger Dryas and/or Preboreal, unrelated to local volcanic activity. Two competing ideas exist for these gullies based on the OSL data, that is formation either (i) driven by sparse vegetation cover and increased surface discharge during the Younger Dryas–Preboreal transition or (ii) driven by linear incision in a more stable, Preboreal landscape.

This study documents, for the first time, how dense the so far largely neglected syn- and post-eruptive gully networks close to the LSV can be. Future studies are required to investigate how different edaphic conditions induced by the gullies (higher bulk density, lower saturated water conductivity) impact vegetation and agricultural crop yields in the area, for example applying a high-resolution, unmanned aerial vehicle (UAV)-based approach (e.g., Bendig et al., 2015; Lussem et al., 2019).

## ACKNOWLEDGEMENTS

Funding by Deutsche Forschungsgemeinschaft (DFG) in the framework of the project “Zur Landnutzung im Umfeld eines römischen Industriereviere” (FI 805/6-1) is gratefully acknowledged. The authors thank land owners and farmers in the Segbachtal for permitting the work on their areas. Aerial images and aerial laser scan data were kindly provided by the State Agency for Geodesy and Geoinformation, Rhineland-Palatinate (Landesamt für Vermessung und Geobasisinformation, Rheinland-Pfalz; LVermGeo). Further support during fieldwork, archaeological interpretation, laboratory analyses and data interpretation was provided by Stefan Wenzel, Rainer Schreg, Martin Grünwald, Holger Schaaff, Veronika Keller, Stefan Maus, Anna Mikulowska, and Michael Burstert. The geomagnetic prospection of the eastern study area was supported by members of the ArchaeoGeoPhysics group, University of Cologne (led by Michael Heinzelmann), that is Dan-Marvin Gluber, Stefanie Hagedorn, Natalie Pickartz, and Janine Seidel. Comments and suggestions by the Editor-in-Chief Stuart Lane, the Review Editor and three anonymous reviewers helped to improve the manuscript and are gratefully acknowledged.

## CONFLICT OF INTEREST

The authors declare that there is no conflict of interest that could be perceived as prejudicing the impartiality of the research reported.

## DATA AVAILABILITY STATEMENT

Data from this article can be made available by the authors upon reasonable request.

## ORCID

Max Engel  <https://orcid.org/0000-0002-2271-4229>

Dominik Brill  <https://orcid.org/0000-0001-8637-4641>

Martin Kehl  <https://orcid.org/0000-0003-4587-5858>

## REFERENCES

- Andres, W., Bos, J.A., Houben, P., Kalis, A.J., Nolte, S., Rittweger, H. & Wunderlich, J. (2001) Environmental change and fluvial activity during the Younger Dryas in central Germany. *Quaternary International*, 79(1), 89–100. [https://doi.org/10.1016/S1040-6182\(00\)00125-7](https://doi.org/10.1016/S1040-6182(00)00125-7)
- Auclair, M., Lamothe, M. & Huot, S. (2003) Measurement of anomalous fading for feldspar IRSL using SAR. *Radiation Measurements*, 37(4-5), 487–492. [https://doi.org/10.1016/S1350-4487\(03\)00018-0](https://doi.org/10.1016/S1350-4487(03)00018-0)
- Beck, N. (2003) Böden. In: Gränitz, F. & Grundmann, L. (Eds.) *Das Mittelrheinische Becken – Eine landeskundliche Bestandsaufnahme im Raum Andernach, Bendorf, Koblenz, Mayen, Mendig, Münstermaifeld und Neuwied*. Böhlau Verlag: Cologne, pp. 21–25.
- Beckmann, T. (1997) Präparation bodenkundlicher Dünnschliffe für mikromorphologische Untersuchungen. *Hohenheimer Bodenkundliche Hefte*, 40, 89–103.
- Bendig, J., Yu, K., Aasen, H., Bolten, A., Bennertz, S., Broscheit, J. et al. (2015) Combining UAV-based plant height from crop surface models, visible, and near infrared vegetation indices for biomass monitoring in barley. *International Journal of Applied Earth Observation and Geoinformation*, 39, 79–87. <https://doi.org/10.1016/j.jag.2015.02.012>
- Blott, S.J. & Pye, K. (2001) GRADISTAT: a grain size distribution and statistics package for the analysis of unconsolidated sediments. *Earth Surface Processes and Landforms*, 26(11), 1237–1248. <https://doi.org/10.1002/esp.261>
- Boden, A.-h.-AG. (2005) *Bodenkundliche Kartieranleitung*. Hannover: BGR.
- Bork, H.-R., Russok, C., Dreibrödt, S., Dotterweich, M., Krabath, S., Stephan, H.-G. & Bork, H. (2006a) Spuren des tausendjährigen Niederschlags von 1342. In: Bork, H.-R. (Ed.) *Landschaften der Erde unter dem Einfluss des Menschen*. WBG: Darmstadt, pp. 115–121.
- Bork, H.-R., Vanwalleghem, T., Dotterweich, M., Schmidtchen, G., Poesen, J., Deckers, J. & Bork, H. (2006b) Verlust und Rückgewinnung von Ackerland: ein Knäuel verfallener Lössschluchten wird entwirrt (Flämisch-Brabant, Belgien). In: Bork, H.-R. (Ed.) *Landschaften der Erde unter dem Einfluss des Menschen*. WBG: Darmstadt, pp. 146–151.
- Chinen, T. & Rivière, A. (1989) Post-eruption Plant Recovery with Reference to Geomorphic Processes in the Summit Atrio of Mt. Usu, Japan. *Geographical Review of Japan, Series B*, 62(1), 35–55. <https://doi.org/10.4157/grj1984b.62.35>
- Chinen, T. & Rivière, A. (1990) Post-eruption erosion processes and plant recovery in the summit atrio of Mt. Usu, Japan. *Catena*, 17(3), 305–314. [https://doi.org/10.1016/0341-8162\(90\)90023-7](https://doi.org/10.1016/0341-8162(90)90023-7)
- Collins, B.D. & Dunne, T. (2019) Thirty years of tephra erosion following the 1980 eruption of Mount St. Helens. *Earth Surface Processes and Landforms*, 44(14), 2780–2793. <https://doi.org/10.1002/esp.4707>
- Collins, B.D., Dunne, T. & Lehre, A.K. (1983) Erosion of tephra-covered hillslopes north of Mount St. Helens, Washington: May 1980–May 1981. *Zeitschrift für Geomorphologie Supplementband*, 46, 103–121.
- Cunningham, A. & Wallinga, J. (2012) Realizing the potential of fluvial archives using robust OSL chronologies. *Quaternary Geochronology*, 12, 98–106. <https://doi.org/10.1016/j.quageo.2012.05.007>

- Degering, D. & Degering, A. (2020) Change is the only constant – time-dependent dose rates in luminescence dating. *Quaternary Geochronology*, 58, 101074. <https://doi.org/10.1016/j.quageo.2020.101074>
- Demoulin, A. & Hallot, E. (2009) Shape and amount of the Quaternary uplift of the western Rhenish shield and the Ardennes (western Europe). *Tectonophysics*, 474(3–4), 696–708. <https://doi.org/10.1016/j.tecto.2009.05.015>
- Dotterweich, M. (2008) The history of soil erosion and fluvial deposits in small catchments of central Europe: Deciphering the long-term interaction between humans and the environment—a review. *Geomorphology*, 101(1–2), 192–208. <https://doi.org/10.1016/j.geomorph.2008.05.023>
- Dotterweich, M. (2013) The history of human-induced soil erosion: Geomorphic legacies, early descriptions and research, and the development of soil conservation—a global synopsis. *Geomorphology*, 201, 1–34. <https://doi.org/10.1016/j.geomorph.2013.07.021>
- Dotterweich, M., Kühn, P., Tolksdorf, J.F., Müller, S. & Nelle, O. (2013) Late Pleistocene to Early Holocene natural and human influenced sediment dynamics and soil formation in a 0-order catchment in SW-Germany (Palatinate Forest). *Quaternary International*, 306, 42–59. <https://doi.org/10.1016/j.quaint.2013.04.001>
- Duller, G.A.T. (2015) The Analyst software package for luminescence data: Overview and recent improvements. *Ancient TL*, 33, 35–42.
- Durcan, J.A., King, G.E. & Duller, G.A.T. (2015) DRAC: Dose rate and age calculator for trapped charge dating. *Quaternary Geochronology*, 28, 54–61. <https://doi.org/10.1016/j.quageo.2015.03.012>
- Galbraith, R.F., Roberts, R.G., Laslett, G.M., Yoshida, H. & Olley, J.M. (1999) Optical dating of single and multiple grains of quartz from Jinmium rock shelter, northern Australia: Part I, Experimental design and statistical models. *Archaeometry*, 41(2), 339–364. <https://doi.org/10.1111/j.1475-4754.1999.tb00987.x>
- Grünewald, M. (2011) Die römischen Gräberfelder von Mayen. *Monographien des RGZM*, 96.
- Grünewald, M. (2012) Reiche Steinbruchbesitzer? Die villa in Axialhofanlage von "Lungenkärchen" bei Mendig (Lkr. Mayen-Koblenz) im Kontext der römischen Landnutzung. In: Grünewald, M. & Wenzel, S. (Eds.) *Römische Landnutzung in der Eifel – Neue Ausgrabungen und Forschungen*. Mainz: Verlag des Römisch-Germanischen Zentralmuseums, pp. 159–179.
- Guerin, G., Mercier, N. & Adamiec, G. (2011) Dose-rate conversion factors: Update. *Ancient TL*, 29, 5–8.
- Hahn, J. & Opp, C. (2011) Geochemische Eigenschaften von Laacher See-Tephra enthaltenden Bodensubstraten in eruptionsnaher und eruptionsferner Position. *Geologisches Jahrbuch Hessen*, 137, 65–77.
- Hensch, M., Dahm, T., Ritter, J., Heimann, S., Schmidt, B., Stange, S. & Lehmann, K. (2019) Deep low-frequency earthquakes reveal ongoing magmatic recharge beneath Laacher See Volcano (Eifel, Germany). *Geophysical Journal International*, 216(3), 2025–2036. <https://doi.org/10.1093/gji/ggy532>
- Hüls, M. (2012) Sedimentäre Untersuchungen zur Rekonstruktion eines vermuteten Wasserbeckens einer Villa rustica in Mendig, Osteifel. BSc Thesis, University of Cologne.
- Huntley, D.J. & Baril, M. (1997) The K content of the K-feldspars being measured in optical dating or in thermoluminescence dating. *Ancient TL*, 15, 11–13.
- Huntley, D.J. & Lamothe, M. (2001) Ubiquity of anomalous fading in K-feldspars and the measurement and correction for it in optical dating. *Canadian Journal of Earth Sciences*, 38, 1093–1106. <https://doi.org/10.1139/e01-013>
- Illies, J.H., Prodehl, C., Schmincke, H.-U. & Semmel, A. (1979) The Quaternary uplift of the Rhenish shield in Germany. *Tectonophysics*, 61(1–3), 197–225. [https://doi.org/10.1016/0040-1951\(79\)90298-1](https://doi.org/10.1016/0040-1951(79)90298-1)
- Janotta, A., Radtke, U., Czwiellung, K. & Heidger, M. (1997) Luminescence dating (IRSL/TL) of Lateglacial and Holocene dune sands and sandy loesses near Bonn, Gifhorn and Diepholz (Germany). *Quaternary Science Reviews*, 16(3–5), 349–355. [https://doi.org/10.1016/S0277-3791\(96\)00103-5](https://doi.org/10.1016/S0277-3791(96)00103-5)
- Kaiser, K., Rother, H., Lorenz, S., Gärtner, P. & Papenroth, R. (2007) Geomorphic evolution of small river–lake-systems in northeast Germany during the Late Quaternary. *Earth Surface Processes and Landforms*, 32(10), 1516–1532. <https://doi.org/10.1002/esp.1480>
- Köhn, M. (1928) Bemerkungen zur mechanischen Bodenanalyse. III. Ein neuer Pipettierapparat. *Journal of Plant Nutrition and Soil Science*, 11(1), 50–54. <https://doi.org/10.1002/jpln.19280110104>
- Kreutzer, S. (2019) fit\_CWCurve: Nonlinear Least Squares Fit for CW-OSL curves [beta version]. Function version 0.5.2. In: Kreutzer, S., Burow, C., Dietze, M., Fuchs, M.C., Schmidt, C., Fischer, M. & Friedrich, J. (Eds.) *Luminescence: Comprehensive Luminescence Dating Data Analysis. R package version 0.9.0.87*. <https://CRAN.R-project.org/package=Luminescence>
- Kreutzer, S., Schmidt, C., DeWitt, R. & Fuchs, M. (2014) The a-value of polymineral fine grain samples measured with the post-IR IRSL protocol. *Radiation Measurements*, 69, 18–29. <https://doi.org/10.1016/j.radmeas.2014.04.027>
- Lang, A. & Mauz, B. (2006) Towards chronologies of gully formation: Optical dating of gully fill sediments from Central Europe. *Quaternary Science Reviews*, 25(19–20), 2666–2675. <https://doi.org/10.1016/j.quascirev.2005.07.021>
- Larsen, A., Bork, H.-R., Fuelling, A., Fuchs, M. & Larsen, J.R. (2013) The processes and timing of sediment delivery from headwaters to the trunk stream of a Central European mountain gully catchment. *Geomorphology*, 201, 215–226. <https://doi.org/10.1016/j.geomorph.2013.06.022>
- Litt, T., Schmincke, H.-U. & Kromer, B. (2003) Environmental response to climatic and volcanic events in central Europe during the Weichselian Lateglacial. *Quaternary Science Reviews*, 22(1), 7–32. [https://doi.org/10.1016/S0277-3791\(02\)00180-4](https://doi.org/10.1016/S0277-3791(02)00180-4)
- Liu, H., Zhang, T., Liu, B., Liu, G. & Wilson, G.V. (2013) Effects of gully erosion and gully filling on soil depth and crop production in the black soil region, northeast China. *Environmental Earth Sciences*, 68(6), 1723–1732. <https://doi.org/10.1007/s12665-012-1863-0>
- Lussem, U., Bolten, A., Menne, J., Gnyp, M.L., Schellberg, J. & Bareth, G. (2019) Estimating biomass in temperate grassland with high resolution canopy surface models from UAV-based RGB images and vegetation indices. *Journal of Applied Remote Sensing*, 13(03), 034525. <https://doi.org/10.1117/1.JRS.13.034525>
- Major, J.J. & Yamakoshi, T. (2005) Decadal-scale change of infiltration characteristics of a tephra-mantled hillslope at Mount St Helens, Washington. *Hydrological Processes*, 19(18), 3621–3630. <https://doi.org/10.1002/hyp.5863>
- Mangartz, F. (1993) Geologie des Hochsteins und seiner Umgebung. In: Bömerich, W. & Mangartz, F. (Eds.) *Der Hochstein – Führer zu einem Vulkan der Osteifel*. Förderverein Kultur- und Heimatmuseum Mendig: Mendig, pp. 1–8.
- Manville, V., Németh, K. & Kano, K. (2009) Source to sink: A review of three decades of progress in the understanding of volcanoclastic processes, deposits, and hazards. *Sedimentary Geology*, 220(3–4), 136–161. <https://doi.org/10.1016/j.sedgeo.2009.04.022>
- Murray, A.S. & Wintle, A.G. (2000) Luminescence dating of quartz using an improved single-aliquot regenerative-dose protocol. *Radiation Measurements*, 32(1), 57–73. [https://doi.org/10.1016/S1350-4487\(99\)00253-X](https://doi.org/10.1016/S1350-4487(99)00253-X)
- Németh, K. & Cronin, S.J. (2007) Syn- and post-eruptive erosion, gully formation, and morphological evolution of a tephra ring in tropical climate erupted in 1913 in West Ambrym, Vanuatu. *Geomorphology*, 86(1–2), 115–130. <https://doi.org/10.1016/j.geomorph.2006.08.016>
- Nowell, D.A.G., Jones, M.C. & Pyle, D.M. (2006) Episodic Quaternary volcanism in France and Germany. *Journal of Quaternary Science*, 21(6), 645–675. <https://doi.org/10.1002/jqs.1005>
- Pagliai, M. & Stoops, G. (2010) Physical and biological surface crusts and seals. In: Stoops, G., Marcelino, V. & Mess, F. (Eds.) *Interpretation of Micromorphological Features of Soils and Regoliths*. Amsterdam: Elsevier, pp. 419–440. <https://doi.org/10.1016/B978-0-444-53156-8.00019-2>
- Patzold, S., Mertens, F.M., Bornemann, L., Koleczek, B., Franke, J., Feilhauer, H. & Welp, G. (2008) Soil heterogeneity at the field scale: a challenge for precision crop protection. *Precision Agriculture*, 9(6), 367–390. <https://doi.org/10.1007/s11119-008-9077-x>

- Poetsch, T. & Altemüller, H.-J. (1990) Die Bildung von Tonbelägen in Böden aus Laacher See Tephra. *Mitteilungen der Deutschen Bodenkundlichen Gesellschaft*, 62, 129–132.
- Rath, S. (2003) Die Erforschungsgeschichte der Eifel-Geologie – 200 Jahre ein klassisches Gebiet geologischer Forschung. PhD Thesis, RWTH Aachen University. <http://publications.rwth-aachen.de/record/59006> (accessed 10 December 2020).
- Reimer, P.J., Bard, E., Bayliss, A., Beck, J.W., Blackwell, P.G., Bronk Ramsey, C. et al. (2013) IntCal13 and MARINE13 radiocarbon age calibration curves 0–50,000 years cal BP. *Radiocarbon*, 55(4), 1869–1887. [https://doi.org/10.2458/azu\\_js\\_rc.55.16947](https://doi.org/10.2458/azu_js_rc.55.16947)
- Reinig, F., Cherubini, P., Engels, S., Esper, J., Guidobaldi, G., Jöris, O. et al. (2020) Towards a dendrochronologically refined date of the Laacher See eruption around 13,000 years ago. *Quaternary Science Reviews*, 229, 106128. <https://doi.org/10.1016/j.quascirev.2019.106128>
- Schmincke, H.-U. (2014) *Vulkane der Eifel*, 2nd edition. Heidelberg: Springer Spektrum. <https://doi.org/10.1007/978-3-8274-2985-8>
- Schmincke, H.-U., Fisher, R.V. & Waters, A.C. (1973) Antidune and chute and pool structures in the base surge deposits of the Laacher See area, Germany. *Sedimentology*, 20(4), 553–574. <https://doi.org/10.1111/j.1365-3091.1973.tb01632.x>
- Schmincke, H.-U., Park, C. & Harms, E. (1999) Evolution and environmental impacts of the eruption of Laacher See Volcano (Germany) 12,900 a BP. *Quaternary International*, 61(1), 61–72. [https://doi.org/10.1016/S1040-6182\(99\)00017-8](https://doi.org/10.1016/S1040-6182(99)00017-8)
- Schmincke, H.-U. & van den Boogard, P. (1990) *Vulkanologische Karte der Osteifel (1:50,000)*. Koblenz.
- Semmel, A. (1996) *Geomorphologie der Bundesrepublik Deutschland*. Stuttgart: Steiner.
- Stolz, C. & Grunert, J. (2006) Holocene colluvia, medieval gully formation and historical land use. A case study from the Taunus Mountains, southern Rhenish Slate Massif. *Zeitschrift für Geomorphologie Supplementband*, 142, 175–194.
- Stoops, G. (2003) *Guidelines for analysis and description of soil and regolith thin sections*. Madison, WI: Soil Science Society of America.
- Strahler, A.N. (1957) Quantitative analysis of watershed geomorphology. *Eos, Transactions American Geophysical Union*, 38(6), 913–920. <https://doi.org/10.1029/TR038i006p00913>
- Stuiver, M. & Reimer, P.J. (1993) Extended  $^{14}\text{C}$  data base and revised CALIB 3.0  $^{14}\text{C}$  age calibration program. *Radiocarbon*, 35(1), 215–230. <https://doi.org/10.1017/S0033822200013904>
- Totschnig, R. & Seren, S. (2011) Archäologisch-geophysikalische Prospektion Segbachtal – “Im Winkel”, Auf dem Lungenkehr, Kreis Mayen-Koblenz/Deutschland (unpublished report). Vienna.
- UMS GmbH. (2012) *Kurzanleitung KSAT*. Munich. Available at: <http://preview.ums.vibrawaagen.de/fileadmin/downloads/KSAT-V1.3.21.zip> (Accessed 12th February 2020).
- USGS. (1996) *Global 30 Arc-Second Elevation (GTOPO30)*. Reston, VA: US Geological Survey (USGS). <https://doi.org/10.5066/F7DF6PQS>
- USGS. (2013) *Landsat 8 OLI/TIRS Surface Reflectance*. Reston, VA: US Geological Survey (USGS). <https://doi.org/10.5066/F787MZJ>
- van den Boogard, P. & Schmincke, H.-U. (1985) Laacher See Tephra: A widespread isochronous late Quaternary tephra layer in central and northern Europe. *Geological Society of America Bulletin*, 96(12), 1554–1571. [https://doi.org/10.1130/0016-7606\(1985\)96<1554:LSTAWI>2.0.CO;2](https://doi.org/10.1130/0016-7606(1985)96<1554:LSTAWI>2.0.CO;2)
- Vanwallegem, T., Bork, H.R., Poesen, J., Schmidtchen, G., Dotterweich, M., Nachtergaele, J. et al. (2005) Rapid development and infilling of a buried gully under cropland, central Belgium. *Catena*, 63(2–3), 221–243. <https://doi.org/10.1016/j.catena.2005.06.005>
- Viereck, L. (2019) Vulkanismus der Osteifel im Umfeld des Laacher Sees (Exkursion D am 25. April 2019). *Jahresberichte und Mitteilungen des Oberrheinischen Geologischen Vereins*, 101, 95–116. <https://doi.org/10.1127/jmogv/101/0004>
- Wallinga, J., Murray, A. & Wintle, A. (2000) The single-aliquot regenerative-dose (SAR) protocol applied to coarse-grain feldspar. *Radiation Measurements*, 32(5–6), 529–533. [https://doi.org/10.1016/S1350-4487\(00\)00091-3](https://doi.org/10.1016/S1350-4487(00)00091-3)

#### SUPPORTING INFORMATION

Additional supporting information may be found online in the Supporting Information section at the end of this article.

**How to cite this article:** Engel M, Dotterweich M, Fülling A, et al. Syn- and post-eruptive gully formation near the Laacher See volcano. *Earth Surf. Process. Landforms*. 2021;1–14. <https://doi.org/10.1002/esp.5119>